EINDHOVEN UNIVERSITY OF TECHNOLOGY

High-rate deposition of microcrystalline silicon p-i-n solar cells in the high pressure depletion regime

Citation for published version (APA):
Smets, A. H. M., Matsui, T., & Kondo, M. (2008). High-rate deposition of microcrystalline silicon p-i-n solar cells in the high pressure depletion regime. *Journal of Applied Physics*, *104*(3), 034508-1/11. Article 034508. https://doi.org/10.1063/1.2961334

DOI:
10.1063/1.2961334

Document status and date:
Published: 01/01/2008

Document Version:
Publisher's PDF, also known as Version of Record (includes final page, issue and volume numbers)

Please check the document version of this publication:

• A submitted manuscript is the version of the article upon submission and before peer-review. There can be important differences between the submitted version and the official published version of record. People interested in the research are advised to contact the author for the final version of the publication, or visit the DOI to the publisher's website.
• The final author version and the galley proof are versions of the publication after peer review.
• The final published version features the final layout of the paper including the volume, issue and page numbers.

Link to publication

General rights
Copyright and moral rights for the publications made accessible in the public portal are retained by the authors and/or other copyright owners and it is a condition of accessing publications that users recognise and abide by the legal requirements associated with these rights.

• Users may download and print one copy of any publication from the public portal for the purpose of private study or research.
• You may not further distribute the material or use it for any profit-making activity or commercial gain
• You may freely distribute the URL identifying the publication in the public portal.

If the publication is distributed under the terms of Article 25fa of the Dutch Copyright Act, indicated by the "Taverne" license above, please follow below link for the End User Agreement:

www.tue.nl/taverne

Take down policy
If you believe that this document breaches copyright please contact us at:

openaccess@tue.nl

providing details and we will investigate your claim.

Download date: 05. Oct. 2023

High-rate deposition of microcrystalline silicon *p-i-n* solar cells in the high pressure depletion regime

A. H. M. Smets,[a] T. Matsui, and M. Kondo
Research Center for Photovoltaics, National Institute of Advanced Industrial Science and Technology, Central 2, 1-1-1 Umezono, Tsukuba, Ibaraki 305-8568, Japan

(Received 27 March 2008; accepted 26 May 2008; published online 11 August 2008)

Hydrogenated microcrystalline silicon films (μc-Si:H) deposited at high deposition rates (~2 nm/s) by means of the very-high-frequency (VHF) deposition technique in the high pressure depletion regime have been integrated into single junction *p-i-n* solar cells. It is demonstrated that μc-Si:H solar cells can be optimized using a twofold approach. First the bulk properties, deposited under steady-state plasma conditions, are optimized by monitoring the presence of crystalline grain boundaries in μc-Si:H. These hydrogenated crystalline grain boundaries can easily be detected via the crystalline surface hydrides contribution to the narrow high stretching modes by infrared transmission spectroscopy. The crystalline grain boundaries suffer from postdeposition oxidation which results in a reduced red response of the solar cell. The absence of these crystalline surfaces in an as-deposited μc-Si:H matrix reflects the device grade microcrystalline bulk material. Second, the prevention of silane backdiffusion from the background during the initial growth is a necessity to deposit a uniform μc-Si:H phase over the entire film thickness. The initial growth is optimized while preserving the optimized bulk properties deposited under steady-state conditions, using initial profiling of plasma parameters such as the silane flow and the VHF power density. Solar cell devices with efficiency of 8.0% at a μc-Si:H deposition rate of 2.0 nm/s are obtained using the presented approach. © *2008 American Institute of Physics*. [DOI: 10.1063/1.2961334]

I. INTRODUCTION

Hydrogenated microcrystalline silicon (μc-Si:H) was introduced as an intrinsic photovoltaic absorbing film in silicon based thin film solar cells in the early 1990s.[1,2] This specific phase of hydrogenated silicon (Si:H) has been integrated in many commercially available thin silicon solar modules since its introduction.[3–8] The enhanced absorption in the infrared[1] (IR) and the optoelectronic stability[2] compared to hydrogenated amorphous silicon (a-Si:H) are the main advantages for integration of μc-Si:H into single junction and multijunction *p-i-n* devices. Solar cells and modules based on a multijunction approach of a-Si:H and μc-Si:H have resulted in conversion efficiencies of cells and modules in the range of 10%–15%.[3–8] To benefit from the enhanced absorption in the red and near IR, thicker intrinsic μc-Si:H films (1–3 μm) are required, compared to a-Si:H (typically 200–400 nm). Consequently, the upscaling of plasma enhanced chemical vapor deposition (PECVD) technologies (high deposition rates of μc-Si:H over large areas) is a crucial issue for the cost reduction in manufacturing photovoltaic products based on thin silicon films.[4] The achievement of higher deposition rates means, in general, increasing the precursor gas flows and plasma power density. This is shown in Fig. 1 (inspired on Fig. 5 in Ref. 9), in which the deposition rate versus power density for device grade μc-Si:H films deposited close to the $a \rightarrow \mu c$ phase transition is plotted. Figure 1 shows all data that could be found in peer reviewed journals.[9–42] Increasing the power density also induces ion-bulk interactions leading to amorphization of the crystalline growth[43,44] and defects.[10,45] In the last 15 years two approaches have been used to suppress this unfavorable effect of ion bombardment during μc-Si:H growth. The first approach is the very-high frequency (VHF) approach (squares in Fig. 1), which is the increase in the electrode bias frequency from the conventional rf bias 13.56 MHz frequency up to 40–150 MHz.[46] VHF enhances the efficiency of silane dissociation in the plasma[47] and drastically reduces the energy of the ions bombarding the grounded deposition sur-

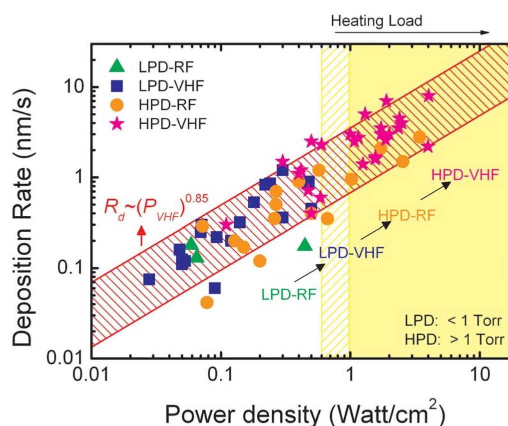

FIG. 1. (Color online) The deposition rate of device grade μc-Si:H (close to the $a \rightarrow \mu c$ phase transition) vs the employed power density (P_{VHF}) for data found in peer reviewed journals (Refs. 9–42). The triangles represent rf-PECVD (13.56 MHz) at low pressure (<1 Torr), the squares represent VHF-PECVD (>13.56 MHz) at low pressure (<1 Torr), the circles represent rf-PECVD at high pressures (>1 Torr) and the stars represent VHF-PECVD at high pressure (>1 Torr). A fit of the data results in a scaling of $R_d \sim (P_{VHF})^{0.85}$. The power density range in which heating of the electrodes by plasma is expected is indicated as well.

[a]Electronic mail: arno.smets@aist.go.jp.

 © 2008 American Institute of Physics

Downloaded 02 Mar 2009 to 131.155.108.71. Redistribution subject to AIP license or copyright; see http://jap.aip.org/jap/copyright.jsp

TABLE I. Deposition series, labeled A–H, with its corresponding conditions (ss for steady state).

Series		SiH_4 (SCCM)	H_2 (SCCM)	Pressure (Torr)	P_{VHF} (W cm^{-2})	Profiling
A	TCO A	12	700	3–12	1.3	⋯
B	TCO A	12	600–850	10	1.3	⋯
C	TCO A	12	600 ss	10	1.3	H_2 profiling 1
D	TCO A	12	600 ss	10	1.3	H_2 profiling 2
E	TCO A	12 ss	600 ss	10	1.3	H_2 profiling 2 +SiH_4
F	TCO A	12 ss	200–1200	10	1.3	SiH_4
G	TCO A	12 ss	600	10	1.3ss	SiH_4+P_{VHF}
H	TCO B	12 ss	600	10	1.3ss	SiH_4+P_{VHF}

face, due to a reduced dc voltage V_{dc}.[48,49] The second approach is increasing the processing pressure up to 5–25 Torr,[11,38] the so-called high pressure depletion (HPD) regime[47] (circles in Fig. 1). This approach reduces the energy of the ion bombardment by many ion-neutral collisions during their acceleration in the collisional plasma sheath.[43] The combined employment of both approaches (stars in Fig. 1), HPD-VHF, has resulted in high deposition rates (2–3 nm/s), while preserving high conversion efficiencies of the *p-i-n* devices.[11,50] The best results of μc-Si:H solar cells deposited in the HPD-VHF regime is η=9.1% at 2.3 nm/s using a conventional shower head electrode,[11] and η=8.7% and 8.5% at 2.7 and 3.1 nm/s, respectively, using the ladder shaped electrode.[50]

Another issue is the fact that "device grade" μc-Si:H is obtained close to transition from *a*-Si:H to microcrystalline silicon ($a \rightarrow \mu c$).[13,14,51] However, unwelcome side effects of high rate deposition in the HPD regime is that the parameter window for device grade μc-Si:H becomes narrower, which enhances the demand for easy optimization strategies and good control of the growth with thickness. Device grade material can be classified as μc-Si:H without any significant postdeposition oxidation, as oxidation is linked to a reduction in the red response of the *p-i-n* device.[11,52,53] The properties of μc-Si:H, such as crystallinity, defects and conductivity have been studied intensively by Raman spectroscopy,[54,55] x-ray diffraction detection,[55,56] transmission electron microscopy,[56] electron spin resonance,[57] and optoelectronic characterization techniques.[58,59] However, these easy-to-use analyze techniques are not able to exclusively determine whether a deposited film is in the good narrow parameter window. The only qualification of device grade material is the time consuming procedure of the integration of the intrinsic film in a *p-i-n* device. Furthermore, in plasma processing it is well known that the *p-i* interface is the most critical interface in a *p-i-n* device. An inferior *p-i* interface is directly reflected in inferior solar cell performance. The control of the initial growth becomes even more crucial for high deposition rates as the characteristic time, in which the properties of the *p-i* interface are determined, becomes shorter. The importance of the *p-i* interface has been shown by inclusion of buffer layers (deposited by hot-wire CVD) between the *p*- and *i*-films[15] and by applying silane profiling during the initial growth phase.[16] These additional processing steps result in improved solar cell performances.

In this paper we present the results on the integration of μc-Si:H, deposited at high deposition rates using the VHF technique in the HPD regime, into *p-i-n* devices. We demonstrate that a fast optimization of the high rate deposited μc-Si:H properties can be obtained by a twofold strategy: First the bulk properties are optimized using the IR analysis of the deposited films. Recently, we have demonstrated that bulk properties of μc-Si:H deposited at high deposition rates can easily be optimized using the hydride stretching mode (SM) signature in the IR spectrum.[60] Second, the initial μc-Si:H growth at the *p-i* interface is optimized using profiling of the deposition parameters just after the plasma ignition. We demonstrate that the control the Si:H phase uniformity with thickness is crucial to obtain good solar cell performances.

II. EXPERIMENTAL DETAILS

In the PECVD deposition configuration used, the upper electrode is a multihole-cathode (MHC) and the bottom electrode is the substrate. More details on MHC-VHF technique can be found in Refs. 12 and 61 The diameter of the electrodes is 13 cm and the typical electrode gap is 6–7 mm for the conditions used in this paper. The 80 MHz output of a signal generator (Kenwood SG5155) is amplified (Thamway T190-6068A) and the resulting bias signal is employed to the MHC cathode and matched (Thamway T020-6068D) to optimize the power coupled into the plasma.

The deposition series (A–H) and the corresponding conditions are presented in Table I. Films have been deposited at a substrate temperature of 180 °C. Initial profiling of the deposition parameters is used for conditions C–G. Initial profiling of the deposition parameter means that the hydrogen flow, silane flow, or the VHF power density has been varied during the initial growth, as depicted in Fig. 2. Hydrogen profiling is the variation of the H_2 flow in the first 180 s after plasma ignition, i.e., ($750 \rightarrow 600$ SCCM) (SCCM denotes cubic centimeter per minute at STP) and ($900 \rightarrow 750 \rightarrow 600$ SCCM) referred to as H_2 profiling I and H_2 profiling II, respectively. Silane profiling is the variation of the SiH_4 flow ($0 \rightarrow 4 \rightarrow 8 \rightarrow 12$ sccm) from 10 s before to 40 s after the plasma ignition. Power profiling is the variation of the VHF power density in the first 35 s ($0.39 \rightarrow 0.78 \rightarrow 1.36$ W cm^{-2}).

Downloaded 02 Mar 2009 to 131.155.108.71. Redistribution subject to AIP license or copyright; see http://jap.aip.org/jap/copyright.jsp

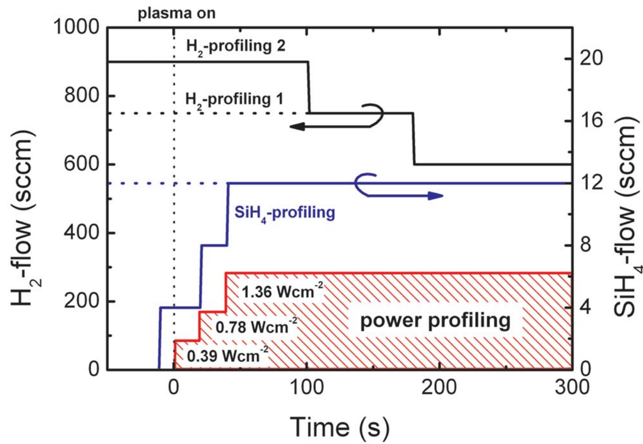

FIG. 2. (Color online) Timing diagram of employed profiling schemes in which several deposition parameters are varied during processing. The hydrogen profiling (I and II), silane profiling and power profiling schemes are depicted.

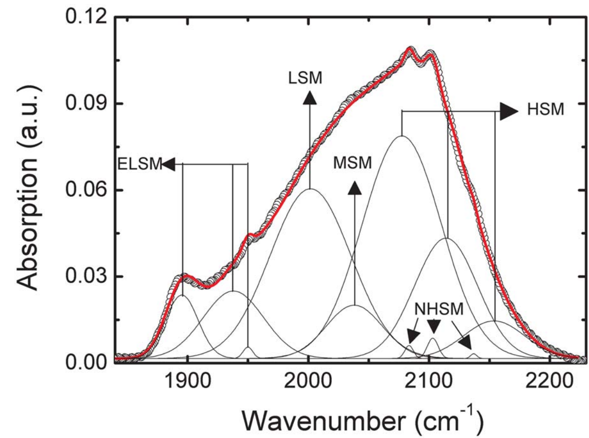

FIG. 3. (Color online) A close-up of the hydride SMs (open circles) in the IR spectrum of a μc-Si:H film. This example of a spectrum shows all possible modes observed for the μc-Si:H phase. The lines correspond to the total fit and the 11 Gaussian shaped SMs. The modes are divided into five groups, the ELSM, LSM, MSM, HSM, and the NHSM.

The μc-Si:H films have been integrated in a solar cell structure of glass/ZnO/p-i-n/ZnO/Ag with an active area of 0.25 cm^2. Note that the texture of the ZnO and the intrinsic film thickness of ~1.8 μm is not optimized and the solar cell structure is exposed to two vacuum breaks, one before and one after the i-layer deposition. Note that an array of 4 $\times$4 solar cells are deposited on a 50$\times$50 mm^2 substrate in which the middle array of 2$\times$2 of solar cells are here referred to as the inner cells. The solar cells were characterized by current voltage (J-V) and spectral response measurements under standard air mass 1.5 (100 mW cm^{-2}) and white-biased monochromatic light illumination.

Single μc-Si:H films are deposited on Corning 1737 samples and on c-Si substrates. Note that the deposition rates obtained on glass or glass/transparent-conducting-oxide (TCO) substrate differ from the deposition rates obtained on c-Si substrates, i.e., the deposition rate on glass is ~10% higher than on c-Si. In this paper we refer to deposition rates determined from films deposited on c-Si films. Conditions A–H result in deposition rates of 1.6–2.0 nm/s. The crystalline volume fraction (X_c) is determined using Raman measurements (Renishaw, He–Ne 633 nm) on μc-Si:H films with thickness of 1.8 μm deposited on Corning 1737 glass (50$\times$50 mm^2) and using the procedure as described by Smit *et al.*[62] The IR spectrum of μc-Si:H films deposited on c-Si (12.5$\times$25 mm^2) is measured using Perkin Elmer Fourier-transform-IR spectrum 2000 in transmission mode. In Fig. 3 a typical IR spectrum showing the bulk hydrides (Si–H–$_x$) SMs is depicted. It is impossible to uniquely resolve all SMs using only one IR spectrum. Nevertheless, by using a large set of samples with a wide variety of Si:H phases, ranging from amorphous up to highly crystalline porous material, we were able to assign a consistent set of SMs capable of fitting the wide variety of spectra measured.[60] The low SM (LSM) (1980–2010 cm^{-1}) and the high SM (HSM) (2070–2100 cm^{-1}) originate from the a-Si:H tissue in the bulk.[63] The HSM range for the μc-Si:H phase broadens by two additional modes: ~2120 and ~2150 cm^{-1}. Furthermore, three narrow HSMs (NHSM, 2083, 2103, and 2137 cm^{-1}) are observed. Unique for μc-Si:H IR spectra is the fact that it can exhibit extreme LSMs (ELSM, ~1895, ~1929, and ~1950 cm^{-1}).

III. RESULTS

A. IR analysis as an optimization tool for the bulk properties

As demonstrated in Ref. 60 a clear relation between the performance of a p-i-n solar cell and the hydride SMs, corresponding to hydrogenated crystalline grain boundaries in the bulk is observed. These crystalline surfaces show post-deposition oxidation and the absence of these surfaces in the μc-Si:H matrix is a crucial requirement for device grade microcrystalline material. In the IR spectrum of μc-Si:H, the presence of crystalline surfaces in the bulk are reflected by the NHSMs at 2083, 2102, and 2137 cm^{-1} corresponding to mono-, di-, and trihydrides at crystalline grain boundaries.[64] When going from a phase with a high crystalline matrix to an amorphous matrix the absorption of the ELSM (~1895, ~1929, and ~1950 cm^{-1}) seems to have its maximum in the phase of μc-Si:H in which the NHSMs are just absent.

The strength of IR analysis as a tool for optimization of μc-Si:H material properties is demonstrated by Fig. 4, in which IR spectra for three different μc-Si:H films with various properties deposited on c-Si are presented. The spectra in Fig. 4 are focused on the range of the dihydride bending modes at 840–890 cm^{-1} and the Si–O–Si SMs at 950–1200 cm^{-1} and the hydride (Si–H–$_x$) SMs. Figures 4(a) and 4(b) represent the IR spectra of a highly crystalline μc-Si:H film deposited under high power and high dilution conditions. The μc-Si:H films have been measured as deposited, 10 days and 10 months after deposition. Figures 4(c) and 4(d) present the IR spectra of μc-Si:H (2.0 nm s^{-1}) when integrated into the p-i-n devices leading to an inferior conversion efficiency of 4.5%. Figures 4(e) and 4(f) present the IR spectra of μc-Si:H (2.3 nm s^{-1}) when integrated into the p-i-n devices leading to conversion efficiency of 9.1%. Note that the films in Figs. 4(c)–4(f) are deposited at high

Downloaded 02 Mar 2009 to 131.155.108.71. Redistribution subject to AIP license or copyright; see http://jap.aip.org/jap/copyright.jsp

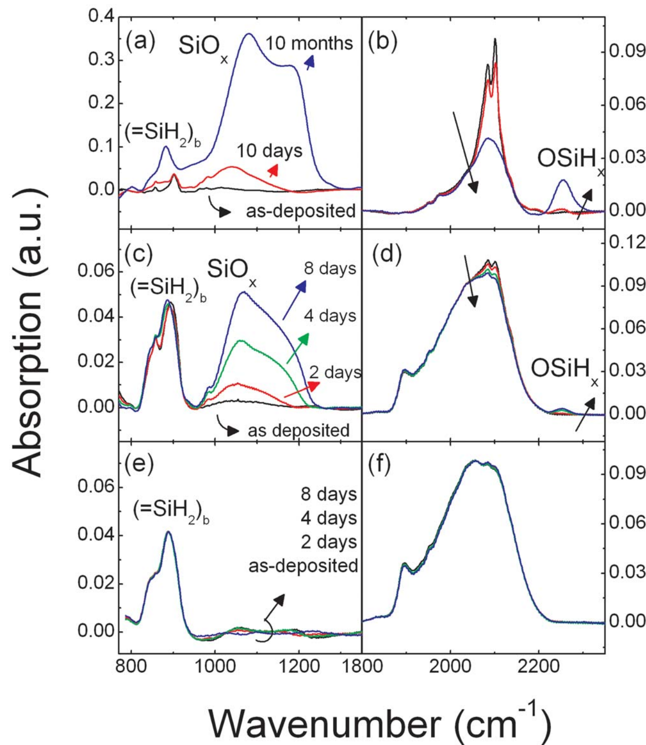

FIG. 4. (Color online) (a) and (b) depict the measured Si–O–Si SMs and the hydride SMs for porous highly crystalline μc-Si:H as deposited, 10 days and 10 months after deposition. (c) and (d) depict the Si–O–Si modes and the hydride SMs for μc-Si:H films, when integrated into a *p-i-n* device, resulting in a conversion efficiency of 4.5% (Ref. 11). (e) and (f) depict the Si–O–Si modes and the hydride SMs for μc-Si:H films, when integrated into a *p-i-n* device, resulting in an conversion efficiency of 9.1% (Ref. 11).

deposition rates using conventional VHF with a flat showerhead electrode.[11] The less dense μc-Si:H [Figs. 4(a) and 4(b)] has a spectrum with a large contribution of NHSMs, which disappears completely within 10 months of exposure to ambient air. Meanwhile the Si–O–Si SMs and a mode around 2250 cm^{-1} appears, corresponding to hydride SMs with oxygen atoms back bonded to the silicon atom O_ySiH_x.[65] This reflects that at least the crystalline grain boundaries within the bulk oxidize and transform to an O_ySiH_x surface. The presence of crystalline grain boundaries and its linked postdeposition oxidation is a signature of inferior material quality, reflected in poor red response of the *p-i-n* device.[52,53] The spectra of intrinsic μc-Si:H, corresponding to inferior efficiency of 4.5% [Figs. 4(c) and 4(d)], still exhibit a small signature of the NHSMs in the IR. The presence of crystalline surfaces is accompanied with postdeposition oxidation in time, reflecting inferior material properties. The NHSMs are absent in the IR spectra of the intrinsic μc-Si:H film corresponding to an efficiency of 9.1% [Figs. 4(e) and 4(f)]. The ELSMs absorption is at its maximum and no postdeposition oxidation of the material is observed, reflecting device grade material. We have used this approach for the first optimization step for the properties of the μc-Si:H bulk deposited using the MHC-VHF setup. The IR spectrum in Fig. 4(f) has been used as a reference representing optimum μc-Si:H bulk properties, as an efficiency of 9.1% is the best result on μc-Si:H single junctions for the 2–3 nm/s deposition range reported so far.[11]

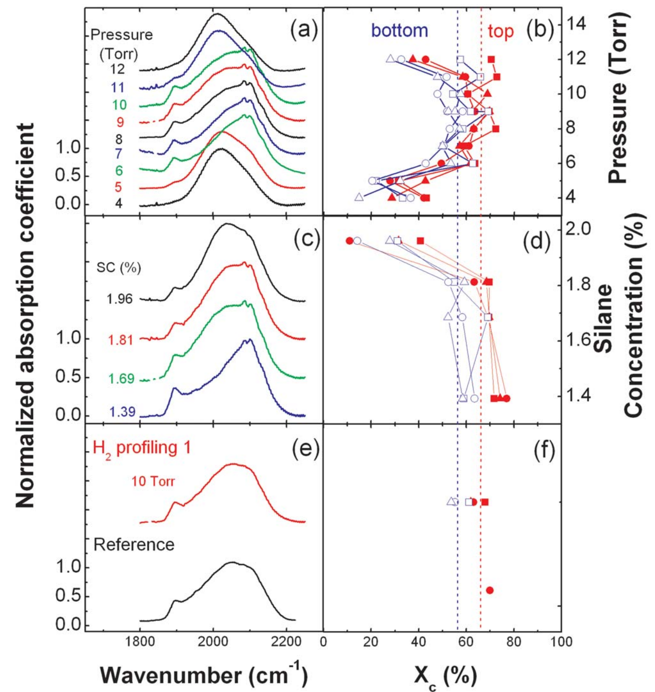

FIG. 5. (Color online) The hydride SMs [(a), (c), and (e)] and the crystallinity fraction X_c [(b), (d), and (f)] determined from the top (solid marks) and bottom side (open marks), respectively. (a) and (b) show the dependence on the pressure (series A), (c) and (d) show the dependence on SC (series B), and (e) and (f) show the results for μc-Si:H obtained using hydrogen profiling I (series C). Note, that in Fig. 4(e) the reference spectrum from Fig. 3(f) is plotted as well. The dotted lines show the crystallinity range in which in general device grade material could be obtained.

B. Optimization of the bulk properties

In Figs. 5(a) and 5(b) the spectra of hydride SMs of the μc-Si:H films as deposited are shown. The crystalline fraction measured from the top (solid data points) and bottom (open data points) of deposition series A (pressure variation) are shown as well. Deposition at low pressures (4 and 5 Torr) results in *a*-Si:H phase having a low crystalline fraction of $X_c < 40\%$. The IR spectra for 4 and 5 Torr exhibit only the broad LSM (1980–2010 cm^{-1}) and the HSM (2070–2130 cm^{-1}) linked to the amorphous phase.[63] The material becomes crystalline X_c(bottom) $> 50\%$ and X_c(top) $> 60\%$ from pressures of 6–10 Torr and the typical microcrystalline SMs signatures show up in this pressure range. Above 10 Torr the films are less crystalline and the SM spectra are free of typical crystalline related SMs such as the ELSMs, NHSMs, and the two additional HSMs. If we consider the spectra of μc-Si:H deposited in the 6–10 Torr regime, we see that all spectra exhibit the NHSMs reflecting inferior material with crystalline grain boundaries. The SMs also show that the Si:H phase transitions around 5–6 Torr and 10–11 Torr are relative sharp, showing the narrowness of the parameter window for optimum material properties.

We have performed many attempts to deposit material without NHSMs at the transition from 5–6 Torr, but it appears to be impossible to deposit material without the unwelcome NHSMs signature at these pressures. Furthermore, the nonremovable NHSMs at 5–6 Torr transition seems to be independent of the electrode used, both MHC and flat show-

Downloaded 02 Mar 2009 to 131.155.108.71. Redistribution subject to AIP license or copyright; see http://jap.aip.org/jap/copyright.jsp

erhead electrodes suffer from the same effect. Therefore, the transition around 10 Torr has been chosen as starting point for further optimization by variation of the hydrogen flow (deposition series B). In Figs. 5(c) and 5(d) the IR spectra and X_c values are shown versus the silane concentration (SC). A decrease in the SC (increasing hydrogen flow) results in a larger crystalline fraction, shown by the higher X_c value and the large dominance of the NHSMs. At SC =1.96% the unfavorable NHSMs almost disappear completely, however, the crystalline fraction drops below 40%, demonstrating a highly nonuniform Si:H phase with thickness and the extreme narrowness of the parameter window for optimum material.

To maintain a high crystalline fraction in the bulk and to obtain IR spectra without NHSMs we have applied a hydrogen profiling step referred to as H_2 profiling I (see Fig. 2): the first 180 s the hydrogen flow is 750 SCCM to guarantee initial crystalline growth and the rest of the deposition the flow is 600 SCCM to avoid the incorporation of crystalline grain boundaries (deposition series C). In Figs. 5(e) and 5(f) the resulting IR spectrum and X_c values are shown. The employment of hydrogen profiling results in an exact replica of the reference IR spectrum from Fig. 4(f), while preserving a high bulk crystallinity fraction $X_c > 60$ at. %, implying that μc-Si:H bulk material without crystalline grain boundaries has been obtained.

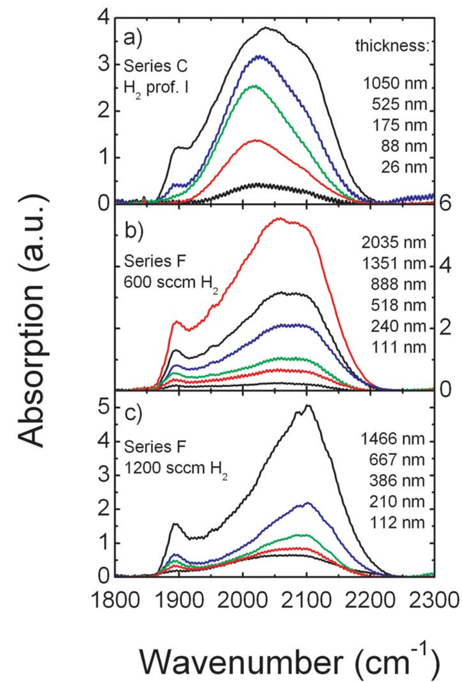

FIG. 6. (Color online) The evolution of the SM spectra with film thickness for series C (a), series F with 600 SCCM H_2 flow (b), and series F with 1200 SCCM H_2 flow (c). The film thickness of the films are depicted in the figure as well.

C. Optimization of the initial growth

The results shown in Fig. 5 are obtained for 1.8 μm thick films. Consequently, information of material properties of the initial growth (<100 nm) cannot easily be resolved. In other words, these spectra do not reveal the uniformity of the μc-Si:H growth with thickness, nor reveal from which thickness the unwelcome crystalline grain boundaries are incorporated. To study the microstructural evolution of the films with thickness, samples with various thicknesses have been deposited under several conditions: hydrogen profiling I (series C), silane profiling using a 600 and 1200 SCCM hydrogen flow (series F). Figure 6(a) shows the evolution of the IR spectra with thickness for the hydrogen profiling I (series C). The IR spectra for the first 525 nm contain two modes: the LSM and the HSM (~2070–2100 cm^{-1}). This implies that the deposited Si:H matrix in the growth of the first 525 nm is dominantly amorphous.[63] For thicker films the IR spectra also exhibit the typical SMs related to the microcrystalline phase. The observed evolution of the IR spectra reflects a highly nonuniform Si:H phase with thickness. These results are consistent with Raman analysis on μc-Si:H films on the Corning glass (simultaneously deposited). Figure 7 shows the X_c values with thickness for series C using hydrogen profiling scheme I. For the first 500 nm the crystalline fraction X_c is below 50% ($X_c < 20\%$ for the first 200 nm). An amorphous incubation layer of some hundreds of nanometers is undesirable in a *p-i-n* device as it will act as an additional barrier in the intrinsic μc-Si:H film.

Several approaches to prevent the growth of a thick initial *a*-Si:H incubation film after plasma ignition have been investigated. The first approach studied is increasing the number of hydrogen profiling steps during the initial growth. If we apply hydrogen profiling step II (see Fig. 2, profiling II has an additional higher H_2 flow step in the first 100 s after plasma ignition compared to hydrogen profiling I) the initial growth becomes more crystalline, as shown in Fig. 7. The second studied approach is employing an initial silane profiling step while keeping the hydrogen flow constant, i.e., a small silane flow of 4 SCCM is turned on just 10 s before plasma ignition, which increased with two steps up to 8 and 12 SCCM at 20 and 40 s after plasma ignition (see Fig. 2). Figure 6(b) shows the evolution of the SM spectra in the IR with increasing thickness for silane profiling condition using a 600 SCCM hydrogen flow (series F). The SM spectra are

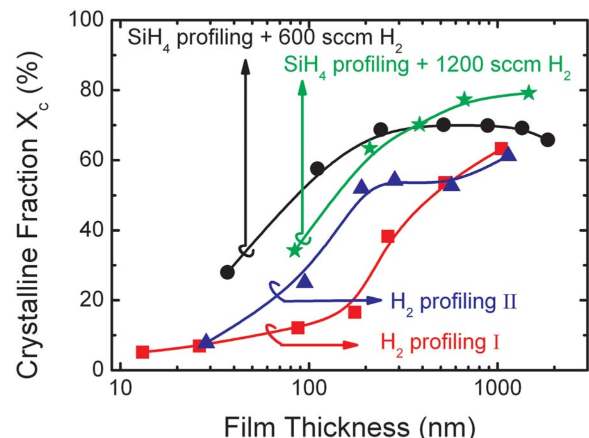

FIG. 7. (Color online) The crystalline fraction X_c vs film thickness for H_2 profiling I (squares), H_2 profiling 2 (triangles), silane profiling with 600 SCCM H_2 flow (circles), and silane profiling with 1200 SCCM H_2 flow (stars).

Downloaded 02 Mar 2009 to 131.155.108.71. Redistribution subject to AIP license or copyright; see http://jap.aip.org/jap/copyright.jsp

an exact replication of that of the reference spectrum in Fig. 4(f) and the shape of the SM spectrum is the same over the entire thickness range. This reflects a rather uniform microcrystalline growth over at least 2 μm. These IR results are again supported by the Raman results in Fig. 7, showing that initial silane profiling lead to an initial crystalline growth and better uniformity in crystallinity over the entire thickness range measured.

Figure 6(c) shows the evolution of the SM spectrum with thickness using silane profiling at a higher hydrogen dilution, i.e., 1200 SCCM hydrogen flow (series F). The appearance of the NHSMs reflects that under this condition the unwelcome crystalline grain boundaries are incorporated. The initial growth reflects the microcrystalline growth of dense material, while after the initial growth the NHSMs can be recognized in the spectra. These observations imply that the crystalline grain boundaries start to incorporate after the initial growth (>200–300 nm). This is also reflected in the X_c values in Fig. 7 (stars). After initial growth the crystallinity increases above 70% up to a value of 80% reflecting highly crystalline material.

Figures 6 and 7 show that to ensure uniform growth of optimum μc-Si:H phase material with thickness, a good control of the initial and steady-state plasma conditions is required. The initial growth of a μc-Si:H film integrated in a solar cell device is very crucial as it determines the properties at the crucial *p-i* interface. Since the unfavorable crystalline grain boundaries characterized by the NHSMs only appear in the IR spectra after the postinitial deposition (>200 nm), the IR spectra of 1.8 μm thick films are suitable to optimize the bulk properties, however, it is hard to resolve information on the initial growth out of measurement on thick films. Therefore, the analysis of an additional thin film of 50–100 nm is required to ensure initial growth close to the $a \rightarrow \mu c$ transition.

D. Integration of high rate μc-Si:H films into solar cells

Films deposited under condition D (hydrogen profiling II) are integrated into *p-i-n* devices. The results of these solar cells are shown by the triangles in Fig. 8 in which the short-circuit current density (J_{sc}), the fill factor (FF), and the efficiency (η) are plotted versus the open-circuit voltage (V_{oc}). The employment of hydrogen profiling does not lead to any reproducibility in the performance of the solar cells deposited at high deposition rates, i.e., the V_{oc}, J_{sc}, FF, and η values show a large scattering and the majority of the cells show a poor performance. Since the IR spectra of these films, deposited using hydrogen profiling, are an exact copy of the reference spectrum, the irreproducibility must have its origin in the amorphous initial growth as depicted in Figs. 6(a) and 7. The best cell performance obtained is V_{oc}=509 mV, J_{sc}=21.4 mA cm^{-2}, FF=0.64, and η=6.9% (see Table II), showing the potential performance of the bulk material under these circumstances.

If we include silane profiling (series E and F) the reproducibility of the solar cell parameters improves significantly as depicted by the open circles in Fig. 8, reflecting a much better control of the initial growth in line with the results shown in Figs. 6(b) and 7. A clear relation between J_{sc} and V_{oc} is obtained for solar cells with V_{oc} values above 480 mV. A decreasing hydrogen dilution in series F corresponds to a decreasing J_{sc} with increasing V_{oc}. The increase in V_{oc} and the decrease in J_{sc} reflect that the amorphous fraction in the film is increasing.[56] To illustrate the relation between IR spectrum and the solar cell performance, the IR spectra of

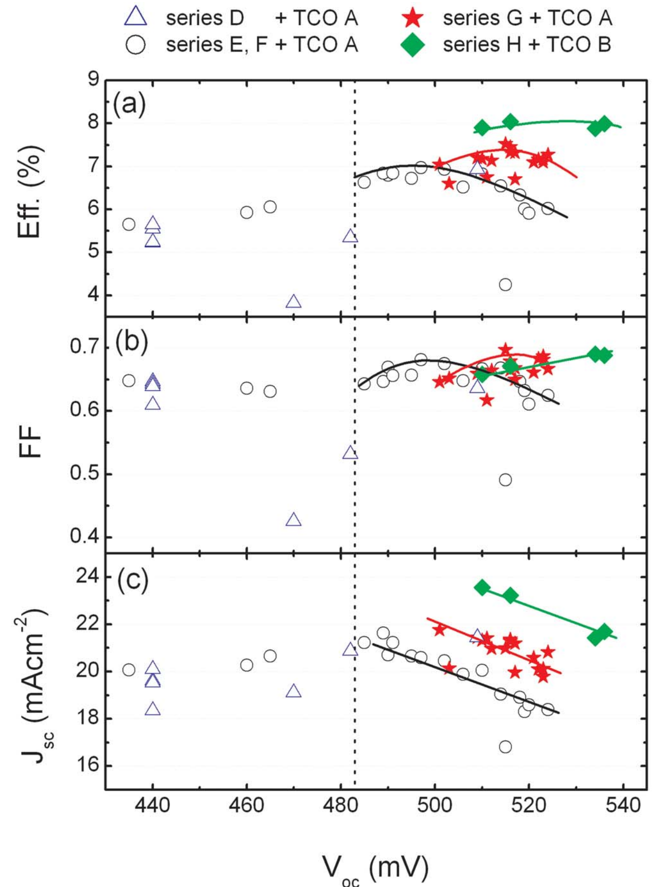

FIG. 8. (Color online) The performance of solar cells expressed in J_{sc}, FF, and conversion efficiency η vs the V_{oc}. The open triangles correspond to H_2 profiling conditions (series D), the open circles correspond to silane profiling conditions (series E and F), the solid stars correspond to silane and power density profiling conditions (series G), and the solid diamonds correspond to silane and power density profiling conditions and using an improved textured TCO B substrate (series H). Note that the variation in V_{oc} for series D, E, and F is caused by variation of the hydrogen dilution (deposition conditions) and cell to cell fluctuations of cells deposited on the same sample area (50×50 mm^2 substrate contains 4×4 cells), while the variation in V_{oc} of series H is caused by cell to cell fluctuations only.

TABLE II. Solar cell performance of *p-i-n* devices in which μc-Si:H films deposited in series D–H are integrated.

Series	V_{oc} (mV)	J_{sc} (mA cm^{-2})	FF	Efficiency (%)
D	509	21.4	0.636	6.9
E	497	20.6	0.68	7.0
F	502	20.5	0.68	6.9
G	515	21.0	0.70	7.5
H (*inner cells*)	536	21.7	0.69	8.0
H (*outer cells*)	516	23.2	0.67	8.0

Downloaded 02 Mar 2009 to 131.155.108.71. Redistribution subject to AIP license or copyright; see http://jap.aip.org/jap/copyright.jsp

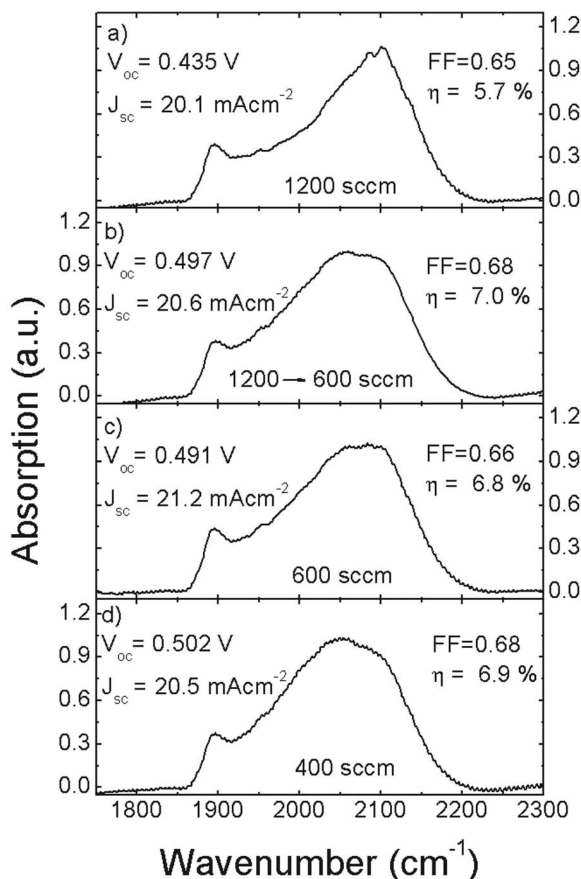

FIG. 9. The SM spectra of films deposited for series F with hydrogen flow of 1200 SCCM (a), 600 SCCM (c), 400 SCCM (d) and series E (b). The performance of solar cells, expressed in V_{oc}, J_{sc}, FF, and η, in which the same films are integrated are depicted as well. The spectra depicted in (b) up to (d) show the narrow range of SM signatures which reflect device grade material.

μc-Si:H films deposited simultaneously on c-Si substrate next to the glass/ZnO/μc-Si:H(p) using silane profiling (series E and F) are depicted in Fig. 9. Figure 9(a) shows that the IR spectrum of μc-Si:H deposited using a 1200 SCCM H_2 flow exhibits NHSMs, reflecting less dense material accompanied with postdeposition oxidation (not shown). The solar cell has a significant reduced performance of η=5.7% in a p-i-n device compared to the lower hydrogen dilution conditions in Figs. 9(b)–9(d), as a result of a reduced red response (not shown) and much lower V_{oc}. The increase in amorphous fraction, (increasing V_{oc} and decreasing J_{sc}), is also reflected by a slight increase in the MSM and LSM with decreasing hydrogen dilution [Figs. 9(b) and 9(c)]. Figures 9(b)–9(d) show the typical narrow range of shapes of the hydride SM spectra, at which solar cells with reasonable material properties can be expected ($V_{oc}>480$ mV). The best cell performance obtained for depositions using silane profiling (series E and F) is V_{oc}=497 mV, J_{sc}=20.6 mA cm^{-2}, FF=0.68, and η=7.0 (see Table II).

If we consider the highest V_{oc} values for μc-Si:H p-i-n devices which are deposited at low deposition rates (540–600 mV),[66] the value of V_{oc}=497 mV is still rather low. This implies that in contrast to condition D, the initial growth is not too amorphous but too crystalline for series F. An additional profiling step of the employed power density was introduced step (deposition series G), to move the deposition conditions during the first 40 s after plasma ignition even closer to the $a \rightarrow \mu c$ transition, while preserving the optimum shape of the SM spectra in the IR. The results of silane and power profiling are depicted in Fig. 8 by the solid stars. Again the same trend is observed, J_{sc} decreases with increasing V_{oc}. In contrast to conditions in which only silane profiling is employed, the V_{oc} values are roughly 20 mV higher at the same J_{sc} values. The cell performance improves compared to series E and F and the best solar cell performance of series G is obtained at higher V_{oc} values: V_{oc}=515 mV, J_{sc}=21.0 mA cm^{-2}, FF=0.697, and η=7.53% for deposition series F (see Table II).

Up to this point we have presented results of solar cells in which we have used homemade ZnO films with a nonoptimized surface texture as a TCO substrate. Finally, we present some results of solar cells in which we have used ZnO films with an improved surface texture (but still not fully optimized), in this paper referred to as TCO B. The intrinsic μc-Si:H film deposited under the same conditions as series G have been integrated in solar cells with TCO B (series H) and the performance is depicted by the solid diamonds in Fig. 8. It is shown that the solar cell performance is further improved by using TCO B. First, higher V_{oc} values could be obtained up to values of 535 mV, showing that a different TCO texture is beneficial to the material properties of the μc-Si:H at the p-i interface. Second, the J_{sc} increases more than 2 mA cm^{-2} at the same V_{oc} compared to series F using TCO A. The best solar cell performances are obtained over a wider V_{oc} range from V_{oc}=516 mV, J_{sc}=23.2 mA cm^{-2}, FF=0.671, and η=8.04% for the outer cells up to V_{oc}=536 mV, J_{sc}=21.7 mA cm^{-2}, FF=0.688, and η=8.00% for the inner cells (Table II). These results reflect a slight inhomogeneity in the Si:H phase around the center of the substrate electrode under condition F. This is confirmed by Raman measurements; the μc-Si:H deposited in a small circular area with diameter of 1.5–2 cm at the center of the electrode has a slightly higher amorphous fraction than outside the center for series H.

We have to address here, that the solar cell performances of MHC-VHF conditions E–H are lower than that of the reference material of 9.1% deposited with the flat showerhead electrode.[11] However, in our view this is not related to the quality of the p-i-n junction part, but to the substrate (no fully optimized TCO used), to the nonoptimized thickness and to the two vacuum breaks before and after the deposition of the intrinsic layer.

IV. DISCUSSION

A. IR analysis as an optimization tool for the bulk properties

The relation between the postdeposition oxidization of μc-Si:H, the incorporated hydrogenated crystalline grain boundaries, and the performance of the p-i-n single junction cells at high rate deposited μc-Si:H demonstrates that significant charge carrier recombination takes place at the crystalline grain boundaries in this material. Since the presence

Downloaded 02 Mar 2009 to 131.155.108.71. Redistribution subject to AIP license or copyright; see http://jap.aip.org/jap/copyright.jsp

of these crystalline surfaces is related to a drop in the red response of the cells,[52,53] the loss of the free charge carriers generated in the crystalline grains must occur at the crystalline grain boundaries. The fact that all crystalline grain boundaries are oxidized in time and transform into O_xSiH_y surfaces suggests that all crystalline grain boundaries have to be surfaces in an interconnected pore and crack network which ends up at the top surface of the μc-Si:H film. The fact that no NHSMs appear anymore in material having the best cell efficiencies suggests that these specific pores with crystalline grain boundaries could be filled with *a*-Si:H tissue or that the crystalline surface is covered by *a*-Si:H tissue. In analogy to *a*-Si:H passivation layer on the *c*-Si surface in heterojunctions,[67,68] the passivation of the crystalline grain boundaries by *a*-Si:H layer could prevent charge carrier recombination at these unwelcome bulk interfaces. It is noteworthy that most of the hydrogen is present in the HSMs, corresponding to macroscopic *a*-Si:H surfaces in the bulk and the LSMs corresponding to vacancies within the bulk of the *a*-Si:H tissue.[63] This fraction of amorphous phase in the bulk does not seem to affect the J_{sc} of the solar cells, which means that the carrier transport in μc-Si:H bulk material is mainly controlled by the crystalline grains. Note, that the hydrogen at the crystalline grain boundaries (contributing to the NSHM) is only a small fraction of the total hydrogen incorporated in the bulk.

If we consider the fact that the contribution of the ELSMs have its maximum for material in which the NHMSs do not appear anymore, could mean that the ELSMs reflect the hydrides in *a*-Si:H tissue squeezed into the pores. The assignment of the ELSMs is still under discussion, however, to explain its rather large frequency shift with respect to the frequency of unscreened monohydrides ($2099\ \text{cm}^{-1}$) and dihydrides ($2124\ \text{cm}^{-1}$) these hydrogen incorporation configurations have to correspond to extreme high local hydride densities combined with possible mutual hydride dipole-dipole interactions.[69] A likely candidate is hydride surfaces standing face to face and which are squeezed in each other. This results in neighboring parallel aligned hydrides, having subsequently opposite dipole directions, which could induce a strong dipole-dipole coupling between the hydride neighbors. Therefore, the ELSM could reflect *a*-Si:H surface pressed on the crystalline grain boundaries or two opposite positioned *a*-Si:H surfaces covering the crystalline grain boundaries.

Note that the μc-Si:H phase still contains many internal surfaces for the device quality material with V_{oc} $=480-540$ mV (Fig. 8), however, all these surfaces are amorphous. These surfaces are represented in the IR spectrum by the three HSMs at 2080, 2120, and $2150\ \text{cm}^{-1}$ and they must reflect macroscopic *a*-Si:H surface in the pores/cracks of the material. The *a*-Si:H tissue is reflected by the LSM ($1980-2010\ \text{cm}^{-1}$) and MSM ($2030-2040\ \text{cm}^{-1}$) assigned to hydrogen in vacancies and the HSM ($2070-2100\ \text{cm}^{-1}$) hydrogen in isolated nanosized voids. Note, that the higher V_{oc} reflects a higher fraction of *a*-Si:H tissue in the μc-Si:H. This shift in Si:H phase is in line with the IR spectra in Fig. 9, which shows that the integrated area of the LSM and MSM, corresponding to *a*-Si:H tissue, are also increasing for the cells having a higher V_{oc}.

Furthermore, it is interesting to mention that μc-Si:H films with crystalline grain boundaries, as reflected by the appearance of NHSMs in the IR spectrum, exhibit reduced electrical properties like reflected in the dark conductivity. Our experience is that for films which have the unwelcome crystalline grain boundaries, the activation energy of the dark conductivity drops below a critical value of ~ 0.5 eV. This is in line with the results obtained by Kočka *et al.*,[70] which showed that grain boundaries deteriorate the charge carrier transport properties. Furthermore, Kočka *et al.* demonstrated that if these unwelcome grain boundaries are incorporated in the films, it happens in the postinitial growth (>500 nm). This seems to be consistent with the incorporation of crystalline grain boundaries as depicted in Fig. 6(c).

B. Optimization of the bulk properties

The transition from the amorphouslike to crystallinelike phase around 5–6 Torr in Figs. 5(a) and 5(b) is caused by a reduction in the energy of the ions bombarding the growth surface during deposition. Around 5–6 Torr the plasma sheath shifts into the collisional regime. Ion bombardment can lead to amorphization of the microcrystalline layer grown via the ion induced bulk-atom displacement. This process is estimated to be activated above a threshold energy of 35 eV (Refs. 43 and 44) for SiH_x^+ ions. Ions gain kinetic energy when they are accelerated to the wall in the plasma sheath and can only lose energy by neutral-ion collisions during their accelerations. If the ion mean free path becomes smaller than the plasma sheath thickness (by increasing pressure) the ion energy is reduced. It seems that from a pressure of 6 Torr the majority of ions cannot gain an energy larger than the threshold energy for ion-bulk-atom displacement. However, it is remarkable that at this transition no material without crystalline grain boundaries can be deposited. If we consider the possible mechanisms responsible for preventing the incorporation of crystalline grain boundaries, it would imply that these mechanisms would require higher pressures. As suggested earlier, possible mechanism could be filling of the pores or passivation of these crystalline surfaces with *a*-Si:H tissue. In view of these types of growth mechanisms higher pressures could induce a higher radical flux to the surfaces within the created pores among the just deposited crystalline grains.

A second transition occurs, going from the crystallinelike phase to the amorphous phase around 10–11 Torr. This transition is most likely caused by a reduction in the atomic hydrogen flux to the deposition surface. Atomic hydrogen is believed to enhance the crystallization of the Si:H growth.[71,72] The net flux of atomic hydrogen to the surface is reduced by additional atomic hydrogen loss in secondary reactions with ions, radicals, and nanoparticles in the plasma phase at these high pressures. Furthermore, the higher pressure could suppress the hydrogen diffusion to the growth surface.

Downloaded 02 Mar 2009 to 131.155.108.71. Redistribution subject to AIP license or copyright; see http://jap.aip.org/jap/copyright.jsp

C. Optimization of the initial growth

The fact that initial silane profiling reduces or prevents the incorporation of an amorphous incubation film implies that at least for conditions without any deposition parameter profiling, the initial plasma conditions differ from plasma conditions during bulk growth, here referred to as the steady-state conditions. Since in steady-state plasma conditions, the injected SiH_4 gas is almost fully dissociated in the plasma zone, the background volume of the reactor is mainly filled with molecular hydrogen. Subsequently, the effective dilution ratio in the plasma zone is determined by the injected SiH_4 and H_2 via the showerhead electrode and H_2 diffusion from the background into the plasma zone. In contrast, when the plasma is ignited, the background volume is (next to H_2) also filled with SiH_4 (without any employment of profiling) and the effective dilution will be smaller compared to the steady-state situation via the additional backdiffusion of the background SiH_4 gas. Consequently, directly after the plasma ignition, the deposition conditions are in a more amorphous phase.[16] The time it takes before the plasma conditions stabilize into the optimized steady-state conditions depends on the residence time of the SiH_4 gas in the background (τ_{res}). This characteristic time depends on the volume of the background, the partial SiH_4 density, and the total flow injected into the chamber. The background volume compared to the plasma zone volume is rather large in our HPD-VHF setup, which makes the deposition at high deposition rates extremely sensitive for this effect. For the HPD-VHF setup the typical residence time of gas in the background is $\tau_{res}=41$, 27, and 21 s at total gas flows of 612, 912, and 1212 SCCM, respectively. If we consider the different approaches of initial deposition parameter profiling, it is easy to grasp that the SiH_4 profiling is better to control the initial SiH_4 backdiffusion compared to H_2 profiling. Although hydrogen profiling slightly decreases the SC compared to no hydrogen profiling conditions, hydrogen profiling does not prevent SiH_4 backdiffusion, but shortens the time scale in which backdiffusion plays a role.

Another issue to be addressed is the fact that different substrate materials could induce different initial μc-Si:H growths, as the IR analysis is performed on μc-Si:H deposited on IR transparent *c*-Si samples and not on glass/TCO/μc-Si:H(p) substrates as used for the solar cells. However, our experience is that the correlation between IR information and the solar cell performances is amazingly sharp as the crystalline grain boundaries reflected by the NH-SMs are only present in the postinitial growth zone (>200 nm). This implies that the substrate material and substrate surface does not affect the incorporation of the unwelcome grain boundaries above a thickness of 200 nm. Moreover, no pretreatment has been performed to remove the native oxide from the *c*-Si films and consequently the growth on this substrate does not start from a crystalline surface.

In this paper the proposed optimization approach is twofold: optimization of the bulk material in the postinitial deposition by preventing the incorporation of the crystalline grain boundaries and optimization of the initial growth by reducing the incorporation of an *a*-Si:H incubation layer, i.e., promoting an instant initial μc-Si:H growth close to the $a \rightarrow \mu c$ phase transition.

D. Integration of high rate μc-Si:H films into solar cells

The employed stepwise increase in the silane flow in the initial growth rules out any effect of silane backdiffusion. However, the question is whether the initial growth is close to the desired $a \rightarrow \mu c$ transition during every initial step. Directly after the plasma ignition, the VHF power density is already fully employed. Since this VHF power density is optimized for the steady-state conditions, the employed power density will be too high for the first silane flow steps (the SC will be lower than in the steady-state condition). A too high power density will result in initial growth which is too crystalline, instead of too amorphous. This is shown by the relatively low V_{oc} values for the *p-i-n* devices deposited under conditions E and F. This effect is partly compensated by the introduction of an additional initial profiling of the VHF power density. The same μc-Si:H bulk material properties are obtained (not shown), while the initial growth is closer to the $a \rightarrow \mu c$ transition. This effect is reflected in Fig. 8 by the trend that around 20 mV higher V_{oc} values are obtained (initial growth dominated) at the same J_{sc} values (bulk dominated) for deposition series G (stars) compared to E and F (circles).

The growth on TCO with an improved (but still not optimized) surface texture results in both higher V_{oc} values at the same current and higher values for the maximum V_{oc} obtained. First of all the improved surface texture improves the light confinement, which results in higher J_{sc} values at the same V_{oc} values. However, this does not yet explain why deposition on TCO B also results in an increase in the maximum V_{oc} obtained. Bailat *et al.*[73] found that the surface morphology of the TCO substrate can affect the initial growth, i.e., it can improve the V_{oc}. In Ref. 74 it is proposed that possible prevention of the incorporation of vertical cracks, induced during the initial growth by "V-shaped" surface morphology of the TCO, by using more "U-shaped" surface morphology is responsible for the improvement in the V_{oc}.

As mentioned in Sec. III D, under deposition series H a slight inhomogeneity over the substrate is observed. The μc-Si:H film deposited in the center of the 50×50 mm^2 sample (circular area with diameter ~ 2 cm, overlapping the 4 middle cells) has a slightly higher amorphous fraction compared to the μc-Si:H outside the center (outer 12 cells). This is reflected in higher V_{oc} values and lower J_{sc} values in the centered cells compared to the outer cells, while the efficiency remains the same. This inhomogeneity is caused by the bulk μc-Si:H deposited during the steady-state conditions. If we assume that atomic hydrogen is the precursor for crystallization, the $a \rightarrow \mu c$ transition should be indicated by a critical value for the ratio between the number of atomic hydrogen atoms arriving at the surface per the number of Si atoms deposited $\Gamma_H/\Gamma_{Si}^{crit}$. The higher the amorphous fraction of the film in the center of the electrode would mean that the Γ_H/Γ_{Si} ratio is smaller than at the edge of the electrode.

Downloaded 02 Mar 2009 to 131.155.108.71. Redistribution subject to AIP license or copyright; see http://jap.aip.org/jap/copyright.jsp

To our knowledge, two possible effects can play a role. First the local effective dilution is determined by the silane and hydrogen gas injected through the shower head and the backdiffusion of the hydrogen molecules from the background volume into the plasma zone. The latter hydrogen supply to the plasma zone results in a slight inhomogeneous hydrogen dilution between the electrodes, i.e., the penetration depth of the backdiffused hydrogen into the plasma zone is limited to roughly 5–6 cm. Consequently, the effective dilution is slightly lower in the center of the electrode, resulting in a locally more amorphous growth.

Second, in a showerhead geometry the local flow velocity of the gas (v_g) depends linearly on the position, i.e., $v_g \sim r$, with r the position from the center. In the center the flow velocity is the smallest, which means the local residence time of the gas and also the SiH_4 precursor is the longest. Consequently, SiH_4 has more chance to dissociate in the center of the electrode (assuming that the longer residence time affects the H_2 dissociation less) and the local flux of deposited Si atoms could be higher, making Γ_H/Γ_{Si} locally lower.

For deposition over significant larger areas, the diffusion effect would only play a role at the edge of the electrodes. For smaller electrodes, this effect does not play a role as long as the penetration depth of the background diffusion is larger than the radius of the electrode. However, a better control over the homogeneity is obtained in a deposition configuration in which the background volume is as small as possible.[75] In contrast, the effect of the flow velocity, if it plays any effect, would be more significant for larger electrodes.

Finally, we would like to make a remark on the IR spectrum of the optimized μc-Si:H deposited using HPD-VHF with a flat shower head [Fig. 4(f)], which we used as a reference for optimum material to optimize the MHC-VHF conditions. An important issue still remaining is how far the occurrence of such a spectrum could be uniquely attributed to optimal material quality. The results in this paper show that the IR spectra of 1.8 μm film successfully reflect the optimized bulk properties and better results are achieved with improved uniformity of the optimized phase with thickness. However, the reference spectrum does not provide any information on the exact initial growth of the μc-Si:H film integrated in the 9.1% record cell. Therefore, it is helpful to mention that this record cell is deposited in a setup with flat showerhead and this setup has a significant smaller background volume compared to the chamber with the MHC installed. This also means that the time to reach the steady-state deposition conditions is much shorter for the deposition setup with the flat showerhead electrode. However, it does not mean that the initial growth as optimized in the setup with MHC exactly reflects the initial growth of the reference material. Therefore, there could still be some room for slight improvements of the initial growth.

V. CONCLUSIONS

High-rate deposited μc-Si:H films using the HPD-VHF technique have been integrated into single junction *p-i-n* solar cell devices. It is demonstrated that a good control of the Si:H phase with thickness is crucial to obtain good device grade material properties at high deposition rates. The initial μc-Si:H growth and the steady-state μc-Si:H bulk growth has been optimized using IR transmission measurements on the hydride vibration and Raman analysis. The optimum bulk material has been found by using the signature of the NHSMs in the IR. The NHSMs correspond to hydrogenated crystalline surfaces, which show postdeposition oxidation and the absence of these surfaces in the μc-Si:H matrix reflect solar grade material. Furthermore, it has been shown that the initial high rate growth conditions can differ significantly from the steady-state high rate conditions for a small sized HPD-VHF geometry within a large background volume. To assure the similar growth conditions during the initial growth as the optimized one during the steady-state growth, initial profiling of the deposition parameters has been employed. Solar cell efficiencies of 8.0% at 2.0 nm/s have been obtained using the presented approach.

[1]C. Wang and G. Lucovsky, Proceedings of the 21st IEEE PVSC, 1990 (unpublished), Vol. 2, p. 1614.
[2]J. Meier, R. Flükiger, H. Keppner, and A. Shah, Appl. Phys. Lett. **65**, 860 (1994).
[3]H. Takatsuka, M. Noda, Y. Yonekura, Y. Takeuchi, and Y. Yamauchi, Sol. Energy **77**, 951 (2004).
[4]A. Shah, J. Meier, A. Buechel, U. Kroll, J. Steinhauser, F. Meillaud, H. Schade, and D. Dominé, Thin Solid Films **502**, 292 (2006).
[5]K. Yamamoto, A. Nakajima, M. Yoshimi, T. Sawada, S. Fukuda, T. Suezaki, M. Ichikawa, Y. Koi, M. Goto, T. Meguro, T. Matsuda, M. Kondo, T. Sasaki, and Y. Tawada, Sol. Energy **77**, 939 (2004).
[6]S. Guha and J. Yang, J. Non-Cryst. Solids **352**, 1917 (2006).
[7]H. Takatsuka, Y. Yamauchi, Y. Takeuchi, M. Fukagawa, K. Kawaruma, S. goya, and A. Takano, Conference Record of the 2006 IEEE Fourth World Conference on Photovoltaic Energy Conversion, 2006 (unpublished), p. 2028.
[8]B. Yan, G. Yue, J. M. Owens, J. Yang, and S. Guha, Conference Record of the 2006 IEEE Fourth World Conference on Photovoltaic Energy Conversion, 2006, (unpublished), p. 1477.
[9]E. A. G. Hamers, M. N. van den Donker, B. Stannowski, R. Schlatmann, and G. J. Jongerden, Plasma Processes Polym. **4**, 275 (2007).
[10]A. Gordijn, M. Vanecek, W. J. Goedheer, J. K. Rath, and R. E. I. Schropp, Jpn. J. Appl. Phys., Part 1 **45**, 6166 (2006).
[11]T. Matsui, A. Matsuda, and M. Kondo, Sol. Energy Mater. Sol. Cells **90**, 3199 (2006).
[12]C. Niikura, M. Kondo, and A. Matsuda, J. Non-Cryst. Solids **338–340**, 42 (2004).
[13]O. Vetterl, F. Finger, R. Carius, P. Hapke, L. Houben, O. Kluth, A. Lambertz, A. Müch, B. Rech, and H. Wagner, Sol. Energy Mater. Sol. Cells **62**, 97 (2000).
[14]Y. Mai, S. Klein, R. Carius, J. Wolff, A. Lambertz, F. Finger, and X. Geng, J. Appl. Phys. **97**, 114913 (2005).
[15]Y. Mai, S. Klein, R. Carius, H. Stiebig, X. Geng, and F. Finger, Appl. Phys. Lett. **87**, 073503 (2005).
[16]M. N. van den Donker, B. Rech, F. Finger, W. M. M. Kessels, and M. C. M. van de Sanden, Appl. Phys. Lett. **87**, 263503 (2005).
[17]J. Kocka, T. Mates, M. Ledinsky, H. Stuchlikova, J. Stuchlich, and A. Fejfar, J. Non-Cryst. Solids **352**, 1097 (2006).
[18]M. Kondo, M. Fukawa, L. Guo, and A. Matsuda, J. Non-Cryst. Solids **266–269**, 84 (2000).
[19]E. Katsia, E. Amanatides, D. Mataras, A. Soto, and G. A. Voyiatzis, Sol. Energy Mater. Sol. Cells **87**, 157 (2005).
[20]K. Saito, M. Sano, S. Okabe, S. Sugiyama, and K. Ogawa, Sol. Energy Mater. Sol. Cells **86**, 565 (2005).
[21]C. Das, T. Jana, and S. Ray, Jpn. J. Appl. Phys., Part 1 **43**, 3269 (2004).
[22]T. Roschek, B. Rech, J. Müller, R. Schmitz, and H. Wagner, Thin Solid Films **451–452**, 466 (2004).
[23]G. Ambrosone, U. Coscia, S. Lettieri, P. Maddalena, and C. Minarini, Mater. Sci. Eng., B **101**, 236 (2003).
[24]A. Takano, T. Wada, M. Shimosawa, S. Fujikake, and T. Yoshida, Jpn. J.

Downloaded 02 Mar 2009 to 131.155.108.71. Redistribution subject to AIP license or copyright; see http://jap.aip.org/jap/copyright.jsp

Appl. Phys., Part 2 **41**, L978 (2002).
[25]M. Tanda, M. Kondo, and A. Matsuda, Thin Solid Films **427**, 33 (2003).
[26]U. Graf, J. Meier, U. Kroll, J. Bailat, C. Droz, E. Vallat-Sauvain, and A. Shah, Thin Solid Films **427**, 37 (2003).
[27]U. Kroll, J. Meier, P. Torres, J. Pohl, and A. Shah, J. Non-Cryst. Solids **227–230**, 68 (1998).
[28]F. Finger, P. Hapke, M. Luysberg, R. Carius, H. Wagner, and M. Scheib, Appl. Phys. Lett. **65**, 2589 (2005).
[29]A. Hadjadj, A. Beorchia, P. Roca I Cabarrocas, L. Boufendi, S. Huet, and J. L. Bubendorff, J. Phys. D **34**, 690 (2001).
[30]E. Amanatides, D. Mataras, and D. E. Rapakoulias, Thin Solid Films **383**, 15 (2001).
[31]L. Guo, M. Kondo, M. Fukawa, K. Saitoh, and A. Matsuda, Jpn. J. Appl. Phys., Part 2 **37**, L1116 (1998).
[32]S. Sumiya, Y. Mizutani, R. Yoshida, M. Hori, T. Goto, M. Ito, T. Tsukuda, and S. Samukawa, J. Appl. Phys. **88**, 577 (2000).
[33]N. Wyrsch, L. Feitknecht, C. Droz, P. Torres, A. Shah, A. Poruba, and M. Vanecek, J. Non-Cryst. Solids **266–269**, 1099 (2000).
[34]B. Rech, T. Roschek, J. Müller, S. Wieder, and H. Wagner, Sol. Energy Mater. Sol. Cells **66**, 267 (2001).
[35]G. Ambrosone, U. Coscia, S. Lettieri, P. Maddalena, M. Ambrico, G. Perra, and C. Minarini, Thin Solid Films **511–512**, 280 (2006).
[36]H. Aguas, P. Roca I Cabarrocas, S. Lebib, V. Silva, E. Fortunato, and R. Martins, Thin Solid Films **427**, 6 (2003).
[37]D. Das and K. Bhattacharya, Jpn. J. Appl. Phys., Part 2 **46**, L1006 (2007).
[38]Y. Sobajima, S. Nakano, T. Toyama, and H. Okamoto, Jpn. J. Appl. Phys., Part 2 **46**, L199 (2007).
[39]Z. Wu, Q. Lei, and J. Xi, J. Mater. Sci. **41**, 1721 (2006).
[40]J. Rudiger, H. Brechtel, A. Kottwitz, J. Kuske, and U. Stephan, Thin Solid Films **427**, 16 (2003).
[41]P. Roca i Cabarrocas, Curr. Opin. Solid State Mater. Sci. **6**, 439 (2002).
[42]P. D. Veneri, L. V. Mercaldo, C. Minarini, and C. Privato, Thin Solid Films **451–452**, 269 (2004).
[43]A. H. M. Smets and M. Kondo, J. Non-Cryst. Solids **352**, 937 (2006).
[44]A. H. M. Smets, W. M. M. Kessels, and M. C. M. van de Sanden, J. Appl. Phys. **102**, 073523 (2007).
[45]C. Niikura, N. Itagaki, and A. Matsuda, Surf. Coat. Technol. **201**, 5463 (2007).
[46]U. Kroll, A. Shah, H. Keppner, J. Meier, P. Torres, and D. Fisher, Sol. Energy Mater. Sol. Cells **48**, 343 (1997).
[47]M. Kondo, Sol. Energy Mater. Sol. Cells **78**, 543 (2003).
[48]M. Heintze, *Amorphous and Microcrystalline Silicon Technology*, MRS Symposia Proceedings No. 467 (Materials Research Society, Pittsburgh, 1997), p. 471.
[49]L. Sansonnes, A. A. Howling, and C. Hollenstein, *Amorphous and Microcrystalline Silicon Technology*, MRS Symposia Proceedings No. 507 (Materials Research Society, Pittsburgh, 1998), p. 541.
[50]Y. Nakano, S. Goya, T. Watanabe, N. Yamashita, and Y. Yonekura, Thin Solid Films **506–507**, 33 (2006).
[51]R. W. Collins, A. S. Ferlauto, G. M. Ferreira, C. Chen, J. Koh, R. J. Koval, Y. Lee, J. M. Pearce, and C. R. Wronski, Sol. Energy Mater. Sol. Cells **78**, 143 (2003).
[52]T. Matsui, M. Kondo, and A. Matsuda, Jpn. J. Appl. Phys., Part 2 **42**, L901 (2003).
[53]T. Matsui, A. Matsuda, and M. Kondo, *Amorphous and Nanocrystalline Silicon Science and Technology*, MRS Symposia Proceedings No. 808 (Material Research Society, Pittsburgh, 2004), Paper No. A.8.1.1.
[54]E. Bustarret, M. A. Hachicha, and M. Brunel, Appl. Phys. Lett. **52**, 1675 (1988).
[55]L. Houben, M. Luysberg, P. Hapke, R. Carius, F. Finger, and H. Wagner, Philos. Mag. A **77**, 1447 (1998).
[56]J. Meier, E. Vallat-Sauvain, S. Dubail, U. Kroll, J. Dubail, S. Golay, L. Feitknecht, P. Torres, S. Fay, D. Fischer, and A. Shah, Sol. Energy Mater. Sol. Cells **66**, 73 (2001).
[57]F. Finger, J. Müller, C. Malten, R. Carius, and H. Wagner, J. Non-Cryst. Solids **266–269**, 511 (2000).
[58]A. Poruba, A. Fejfar, Z. Remeš, J. Špringer, M. Vaněček, J. Kočka, J. Meier, P. Torres, and A. Shah, J. Appl. Phys. **88**, 148 (2000).
[59]J. Kočka, T. Mates, M. Ledinský, H. Stuchlíková, J. Stuchlík, and A. Fejfar, Thin Solid Films **516**, 4966 (2008).
[60]A. H. M. Smets, T. Matsui, and M. Kondo, Appl. Phys. Lett. **92**, 033506 (2008).
[61]C. Niikura, N. Itagaki, M. Kondo, Y. Kawai, and A. Matsuda, Thin Solid Films **457**, 84 (2004).
[62]C. Smit, R. A. C. M. M. van Swaaij, A. M. H. N. Petit, W. M. M. Kessels, and M. C. M. van de Sanden, J. Appl. Phys. **94**, 3582 (2003).
[63]A. H. M. Smets, W. M. M. Kessels, and M. C. M. van de Sanden, Appl. Phys. Lett. **82**, 1547 (2003).
[64]V. A. Burrows, Y. J. Chabal, G. S. Higashi, K. Raghavachari, and S. B. Christman, Appl. Phys. Lett. **53**, 998 (1988).
[65]M. Niwano, J. Kageyama, K. Kurita, K. Kinashi, I. Takahashi, and N. Miyamoto, J. Appl. Phys. **76**, 2157 (1994).
[66]M. N. van den Donker, S. Klein, B. Rech, F. Finger, W. M. M. Kessels, and M. C. M. van de Sanden, Appl. Phys. Lett. **90**, 183504 (2007).
[67]S. De Wolf and M. Kondo, Appl. Phys. Lett. **90**, 042111 (2007).
[68]M. Tanaka, M. Taguchi, T. Matsuyama, T. Sawada, S. Tsuda, S. Nakano, H. Hanafusa, and Y. Kuwano, Jpn. J. Appl. Phys., Part 1 **31**, 3518 (1992).
[69]A. H. M. Smets and M. C. M. van de Sanden, Phys. Rev. B **76**, 073202 (2007).
[70]J. Kočka, H. Stuchliková, J. Stulík, B. Rezek, T. Mates, V. Švrček, P. Fojtík, I. Pelant, and A. Fejfar, J. Non-Cryst. Solids **299–302**, 355 (2002).
[71]H. Fujiwara, M. Kondo, and A. Matsuda, J. Non-Cryst. Solids **338–340**, 97 (2004).
[72]S. Sriraman, S. Agarwal, E. S. Aydil, and D. Maroudas, Nature (London) **418**, 62 (2002).
[73]J. Bailat, D. Dominé, R. Schlüchter, J. Steinhauser, S. Faÿ, F. Freitas, C. Bücher, L. Feitknecht, X. Niquille, T. Tscharner, A. Shah, and C. Ballif, Proceedings of the Fourth WCPEC Conference, Hawaï, 2006 (unpublished), p. 1533.
[74]M. Python, E. Vallat-Sauvain, D. Dominé, L. Fesquet, A. Shah, and C. Ballif, J. Non-Cryst. Solids **354**, 2258 (2008).
[75]A. A. Howling, B. Strahm, P. Colsters, L. Sansonnens, and Ch. Hollenstein, Plasma Sources Sci. Technol. **16**, 679 (2007).

Downloaded 02 Mar 2009 to 131.155.108.71. Redistribution subject to AIP license or copyright; see http://jap.aip.org/jap/copyright.jsp